

On the Evolution of Amplitude Modulated Excitation in Still Air

Tal Yehoshua* and Avi Seifert**

School of Mechanical Engineering Faculty of Engineering, Tel-Aviv University, Ramat-Aviv
69978, Israel

ABSTRACT

Active flow control that is coupled with flow instability has the potential to be energy efficient. However, many applications especially those characterized by large dimensions and low speeds dictate Strouhal numbers which require low frequencies, typically below 100Hz. These frequencies can be orders of magnitude smaller than the efficient operating frequency of common zero-mass-flux actuators. Therefore, the effects of different excitation modes, capable of generating low frequencies from actuators resonating at much higher frequencies, were studied experimentally. The excitation signals included a pure sine wave (as a reference) and amplitude modulated sine wave, in order to generate low frequency excitation through nonlinearity. Detailed particle image velocimetry (PIV) and hot wire measurement are presented and discussed.

The findings of the current study show that when the actuator operates in still air and is excited by a pure sine wave, the nominally 2D excitation creates a train of quasi-2D vortex pairs. The vortex-pairs are created by the high-shear at the edges of the ejected flow during the blowing stage of the cycle, provided that a threshold slot exit Strouhal number is exceeded. The vortex convection speed approximately scales with the peak velocity at the slot exit. Two main mechanisms were identified as responsible for low frequency generation from amplitude modulated signals. The first mechanism is attributed to Sub-critical vortices, generated as part of a modulated strength vortex train, are ingested back into the actuator and do not affect the far field. The second mechanism is related to vortex pairing. In this scenario, larger circulation, faster convecting vortices accelerate and amalgamate with slower, weaker vortices to form one vortex pair that affects the far field. As a result of both mechanisms, the far-field senses a signal that is dominated by the low frequency modulation.

1. INTRODUCTION

Zero-Mass-Flux (ZMF) actuators (commonly known also as “Synthetic jets”) create oscillatory momentum and unsteady vorticity flux, are considered versatile tool for active flow control (AFC), with applications such as separation control, thrust vectoring, mixing and heat transfer enhancement and more (Ref. 1-7). Typically, these devices are used to generate large coherent structures in shear flows, promoting transition, introducing unsteady harmonic or pulsating motion into a turbulent shear flow or even generating turbulent jets through entrainment of still fluid. In the latter application it is physically relevant to use the term “synthetic jets” (Ref. 4), used nowadays for AFC actuation in general.

From the time that Crow and Champagne (Ref. 8) investigated the orderly structures in turbulent jets, the dynamics of artificially excited jets aroused great interest in the scientific community. Pulsed jets were also used in industrial applications in internal combustion engines for improving the mixing of fuel and air (Ref. 2). The separation of boundary layers from lifting bodies could be delayed, thereby generating higher lift and lower drag (compared to the uncontrolled baseline) when oscillatory momentum is introduced to the flow (Refs. 3 and 6). Though it was clearly demonstrated that periodic excitation is a useful tool for Active Flow Control (AFC), the understanding of the physical mechanism governing the interaction of periodic excitation with ambient, stagnant or flowing fluid is far from being complete. Only partial understanding of how large amplitude disturbances create coherent structures in common flows, the receptivity problem, exist (Ref. 9). The effects of the boundary

* Graduate Student, ** Professor, seifert@eng.tau.ac.il

conditions (especially the excitation direction, the comparison between holes and slots and the form of the excitation signal) on the actuator performance and features of the resulting coherent structures, and their effects on the controlled flows are not thoroughly documented or understood.

Zero-mass-flux fluidic actuator, typically contain three components: Active materials (such as Piezo ceramic disks) attached to a membrane(s), a cavity and a slot, communicating the cavity and the surrounding fluid. Several configurations were tested and reported in the literature and reviewed by Cattafesta and Sheplak (Ref. 30), and a schematic of a compact design is shown in Fig. 1. When the Piezo element is driven by an alternating (AC) voltage, the membrane oscillates between two extreme conditions as shown schematically (and in an exaggerated manner) in Fig. 1. Due to the pressure oscillations that are generated in the actuator's cavity, velocity oscillations (with a mean of zero) are generated at the exit slot. During the suction stage (Fig. 1b), fluid is drawn into the cavity from the surrounding fluid, stagnant in this case. While during the blowing stage of the cycle, strong shear layers are formed between the exhaled and the surrounding still air. In the absence of external flow, and as a consequence of the vorticity flux of the strong shear layers ejected from the actuator's slot, in an intermittent manner, two counter rotating vortices (which are, after all, a part of an elliptic vortex ring due to the finite length of the slot, Refs. 32 and 33), are created at the "lips" of the slot, and propagate downstream alongside the high velocity slug ejected during the blowing stage of the cycle.

By the time the suction stage begins, and for supercritical slot exit peak velocities (Refs. 17, 25-28), the vortex pair has already propagated far enough from the slot not to be inhaled back into the slot. This condition is satisfied provided the vortex-pair advection velocity, U_c , is greater than the suction velocity at the vortex core location at any given time. In Ref. 28 it was shown that the convection speed of the velocity slug and vortex pairs are similar and about 0.21 to 0.29 of the peak slot exit velocity, slightly increasing with the excitation Reynolds number. The time periodic reversal in the flow direction creates a stagnation point in the vicinity of the slot (that would lay on the centerline of a symmetric actuator operating in still air) and the location of this stagnation point varies with time when considering a phase-locked averaged velocity field. Indeed, it was demonstrated (Ref. 4) that the distance of this stagnation point from the slot increases with L_0/h (excitation amplitude). With L_0 defined as the stroke length, the distance the velocity slug travels during the expulsion stage, assuming 2D flow and h being the slot width. The magnitude of the asymmetry between the blowing and suction stages of the actuator operation, at a certain distance from the slot, increases with the peak slot exit velocity (U_p or L_0/h) and could be considered a non-linearity of the system (Refs. 12, 3, 28) resulting also in thrust generation. Holman et al (Ref. 27) suggested that the critical Reynolds (or Strouhal) number can be approximated by the square of the Stokes number for a 2D slot, leading to $U_{p,cr} \approx 4\pi f h$ in the current case.

Of special interest are cases in which the actuators' output is coupled with a natural instability of the flow (Refs. 1, 3). This condition allows enhanced effectiveness, since the flow instability amplifies the unsteady motion induced by the actuator. Typically, the mechanical and Helmholtz resonance frequencies of the actuator (where their output is significant) are at much higher frequencies than the unstable frequencies of the base flow to be controlled, when the actuator size is maintained small for low weight, cost and energy expenditure, at least at low speeds and large dimensions (e.g., general aviation airplane at take-off). In order to efficiently excite the flow, it is desirable to create excitation at these low unstable frequencies. It is electrically and mechanically possible to use amplitude modulation or burst mode (Ref. 29, 6) as an excitation input. It was recently shown (Refs. 6, 11 and 22) that burst mode, using low duty cycles, leading to extremely low momentum coefficients, are very effective for flow control applications. It was demonstrated (Refs. 29, 6, 11, 22) that the far field was affected only by the modulation frequency even though it is produced by the high frequency excitation. The earlier studies (Refs. 29, 6) do not provide an explanation nor hypothesize the mechanism generating low frequency excitation from the AM signal. It was later suggested (Refs. 11, 22) that a wide excited spectrum is obtained due to the pulsatile nature of the excitation. Therefore, it becomes feasible for the base flow to amplify the frequencies it is most unstable to and use the control input effectively.

The aim of this paper is to demonstrate and attempt to explain flow features generated by ZMF actuators using amplitude modulated excitation signals for two relevant exit slot boundary conditions. The manner in which the boundary and operating conditions affect the resulting velocity slug (ejected during the blowing stage of the cycle), the train of vortex pairs and their interaction with the surrounding still fluid and with each other are studied and discussed. Particle Image Velocimetry (PIV),

Hot-wire (HW) anemometry and unsteady pressures were the main measurement tools. The current study is limited to excitation of still fluid as a first stage in understanding the excitation interaction with a boundary layer flow. For wall normal excitation, with large ratio of excitation magnitude to free-stream velocity (order unity and larger), the near wall vortex dynamics will be dominated by the excitation parameters. Besides the additional fundamental challenge in explaining this complex flow, applications exist and will be found where low frequency excitation will be required. Common high frequency actuators are more efficient and compact than actuators capable of directly creating low frequency, dictating large scale actuators.

The paper is divided into the following sections. The experimental set-up is described in Sec. 2, results are provided in Sec. 3, discussing the effects of amplitude modulation using two actuator boundary conditions. Conclusions are provided in Sec. 4.

2. EXPERIMENTAL SET-UP

Actuators

Experiments were performed on two types of actuators. The compact actuator (hereafter, CA) experiments were performed on a small, anodized, metallic actuator having dimensions of 46mm x 48mm and 4mm thickness (as shown schematically in Fig. 1). A slot of 1mm (wide) by 39mm (long) connects the cavity with the external fluid. Additional actuators were designed, fabricated and characterized for the excitation-boundary layer interaction experiments (Ref. 17), but here only the operation of the 90° actuator in still air will be discussed. The 90° actuator had a span uniform cavity, driven at the Helmholtz resonant frequency (about 1 kHz). The slot was 1mm wide by 135mm long. The actuator to be discussed here ejected the excitation normal to the wall on which it was installed. Figure 2 presents the 90 deg actuator boundary conditions and the axis system. The structures of the CA and the 90deg actuators are similar with the main difference being the presence of the wall normal to the excitation direction for the 90 deg actuator. As we shall see later, the different slot exit boundary

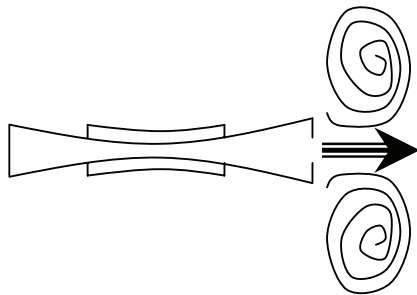


Figure 1a. Schematic principle of operation of compact, cavity installed Piezo actuator. Blowing stage.

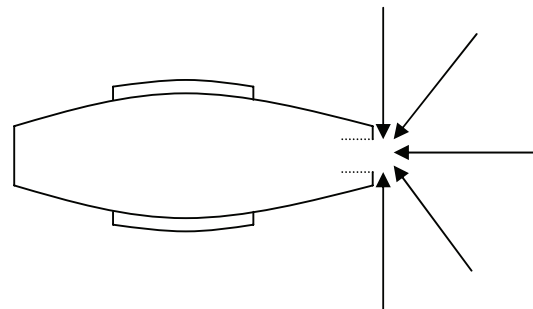


Figure 1b. Schematic principle of operation of compact, cavity installed Piezo actuator. Suction stage.

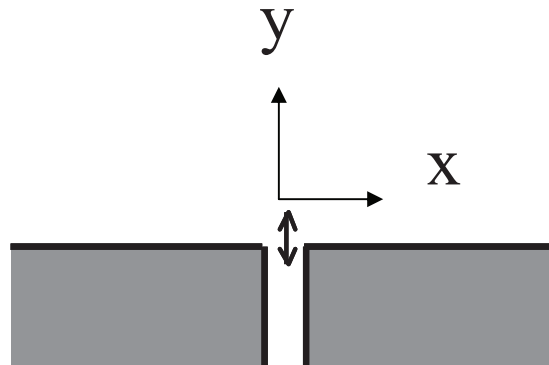


Figure 2. The 90 deg actuator boundary condition. Origin of axis system is at slot exit. Z is positive out of the page.

condition has no measurable effect on the evolution of the vortices. Figure 3 shows a picture of this actuator installed above a small wind tunnel test section (Ref. 17, 25). Note that there is a significant difference between the boundary conditions of the compact actuator and the 90° , plate inserted actuator, namely a 360° vs. 180° in-plane suction into the slot and fluid entrainment capability during the ejection stage. However, the resulting flow fields were quite similar. Unsteady pressure and temperature were measured in the 90° actuators' cavity. Indications of the actuator membrane displacements were measured for health monitoring purposes, using part of the Piezo element as a displacement sensor.

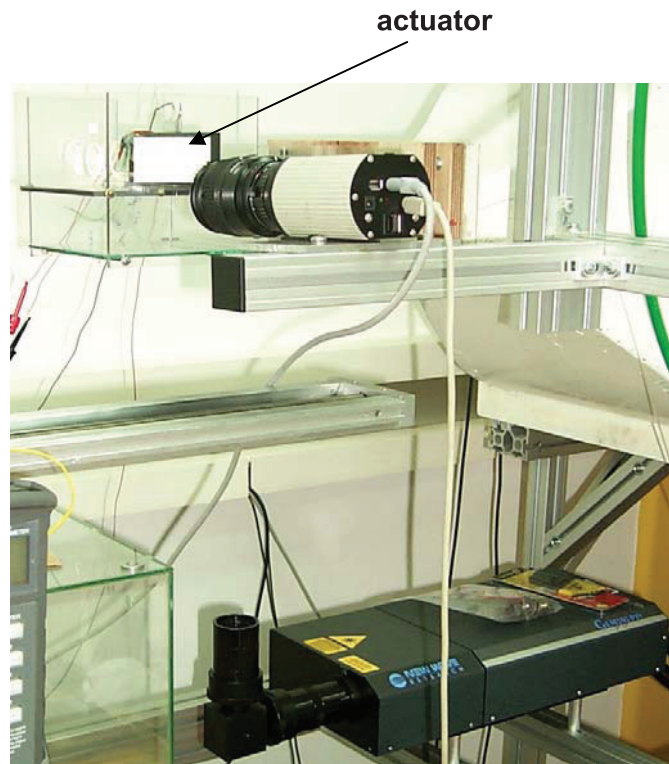


Figure 3. The 90° actuator installed above small wind tunnel test section. Flow is to the left. Laser and Light sheet forming optics are shown below.

Particle Image Velocimetry (PIV) Set-up

The flow fields generated by the actuators were measured using a two-component PIV system, with a double pulsed Nd:Yag laser, operating below the maximum output of 200mJ/pulse. The laser wavelength was 532nm with a maximum repetition rate of 15Hz. Light-sheet thickness was about 1mm.

The images were acquired using a double exposure CCD camera with a resolution of 1300 x 1030 pixels and a maximum sampling rate of 12 Hz. The camera was placed perpendicular to the light-sheet. A schematic description of the experimental setup for measuring the compact actuator output in still air is shown in Fig. 4. The dimensions of the glass container were 450mm x 450mm (base area) x 500mm (height).

Seeding particles for the compact actuator experiments were produced by an atomizer, creating water droplets on the order of $1\mu\text{m}$. The particles were fed into the test chamber from a small opening. Once the required density and distribution were achieved, the seeding was stopped, in order not to affect the flow field. The 90° actuator was tested as installed in the plate test section of the small wind tunnel. The actuator was characterized in still air, in which seeding was provided by a theatrical smoke generator. The smoke source was positioned at the entrance to the small wind tunnel (on the right side of Fig. 3). PIV data was processed using commercial software and a rectangular grid with a minimum of 24 by 24 pixels per interrogation region.

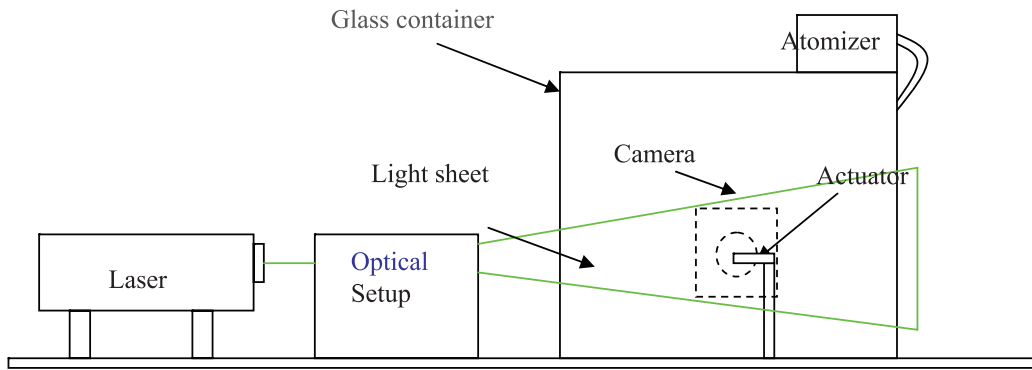


Figure 4. Compact Actuator PIV test set-up.

Actuator Characterization

A comprehensive bench-top calibration was performed, in order to evaluate the fluidic output of the actuators. These tests included frequency response at several excitation levels using either a pure sine or frequency sweep signals and amplitude scans at selected frequencies. The mechanical resonance frequencies of each active element were easily identified using a feedback sensor that was a part of the Piezo element. The 90° actuator also included a thermocouple and an unsteady pressure sensor installed at the bottom of the cavity, opposite the exit slot and at mid span. A calibrated hot-wire (1-60m/s, uncertainty of 2%) was placed in the core region of each exit slot, and the velocity signal was measured for the relevant range of excitation frequencies, typically between 0.3kHz to 2.5kHz. Figure 5a shows a frequency scan conducted at five span (z) locations ($x=y=0$) of the 90° actuator. The peak exit velocities are plotted along with the actuator’s cavity pressure fluctuations (right side ordinate) against the excitation frequency. Two resonance frequencies can be identified: the lower one corresponds to the Helmholtz resonance while the higher to the active element’s mechanical resonance. Note the superior spanwise uniformity, though at lower peak exit velocities, of the Helmholtz frequency. No attempt was made to unify the mechanical resonance of the active elements exciting the cavity. Due to its superior 2D performance the cavity Helmholtz frequency was selected as the working frequency. Figure 5b presents amplitude scans of the 90° actuator, showing peak slot exit velocity versus cavity pressure oscillations, at the same locations as in Fig. 5a, performed at the Helmholtz resonance frequency of 1060Hz. One can note two slopes for the peak velocity vs. actuator’s cavity pressure amplitude plots. The slope change occurs at $U_p \approx 12$ m/s. A similar behavior was observed previously (Refs. 3 and 12). The change in slope is attributed to the threshold U_p for the “escape” of the vortex pairs from the vicinity of the slot (Refs. 25-26) and is clearly a non-linear phenomenon. Seifert and Pack (1999, Ref. 3) provide dimensional considerations indicating that at low P' (actuator cavity pressure fluctuations),

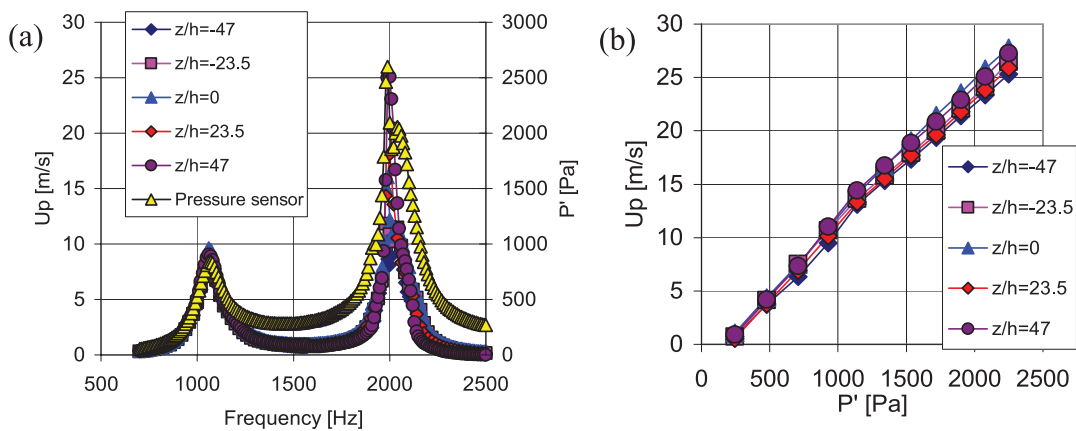


Figure 5. Actuators calibration data. Frequency scan of the 90° actuator (a), Amplitude scan of the 90° actuator at $x=y=0$ and at the acoustic resonance frequency, (1060Hz), conducted at five spanwise locations (b).

$U_p \propto P'$ while at large P' , $U_p \propto (P')^{1/2}$. Holman et al (Ref. 27) provide scaling arguments that predict a Strouhal-Reynolds correlation for the formation of synthetic jets. For the current test conditions, $U_{p,cr} \approx 18.8\text{m/s}$ for the CA and 13.3m/s for the 90deg actuator, is calculated from the Strouhal-Reynolds critical value for jet formation while no vortices “escape” the slot at lower U_p . The spanwise uniformity of the excitation, at the Helmholtz resonance frequency, is better than $\pm 10\%$, including hot-wire calibration and positioning uncertainty.

In addition to a pure sine (PS) input excitation signal, amplitude modulation (AM) input waveform was tested. Figure 6 (reproduced from Ref. 11) shows the excitation, pressure and de-rectified slot exit velocity signal. As noted before (Ref. 11), the velocity signals do not perfectly follow the excitation signals, due to the 2nd order dynamic system features of the actuator, operating at the Helmholtz frequency.

The parameters defining the AM signal are the carrier frequency – f_r (in our case $\sim 1\text{kHz}$, the Helmholtz resonance frequency of the actuators), the modulation frequency – f_m and the peak amplitude along a modulation period cycle – A_p , namely three parameters – f_r , f_m and A_p .

Figure 6 presents two voltage excitation waveforms and corresponding velocity signals that were measured at the actuator’s slot exit by a hot-wire. If one applies a pure sine excitation voltage to the Piezo elements, the pressure oscillation in the cavity as well as the velocity signal at the slot track the excitation waveform and frequency as shown in Fig. 6(a). This also holds for the amplitude modulation waveform as shown in Fig. 6(b), with the reservation that as f_m approaches f_r , the resulting U_p will not arrive to its steady-state value and increasing phase-shift will also develop. The system dynamics are dictated by the frequency ratio f_r/f_m . Only if this ratio is large enough, transient effects would not dominate the output. For this reason we have focused our attention on the AM signal and selected operating conditions which are not dominated by transients. The transient period of the actuator typically lasts 3-5 cycles. Therefore, as long as $f_r/f_m > 5$ the modulation could be used and transient effects resulting from the actuator dynamics are not dominant.

3. DISCUSSION OF RESULTS

The evolution of wall-normal excitation in still air

Figures 7a-e present four phases of the measured flow field generated by the 90° actuator operated by pure sine excitation at 1060Hz and peak slot exit velocity $U_p = 18\text{m/s}$, alongside a schematic of the signal time history. Figure 7a, indicates the phase of each of the flow fields presented in Figures 7b

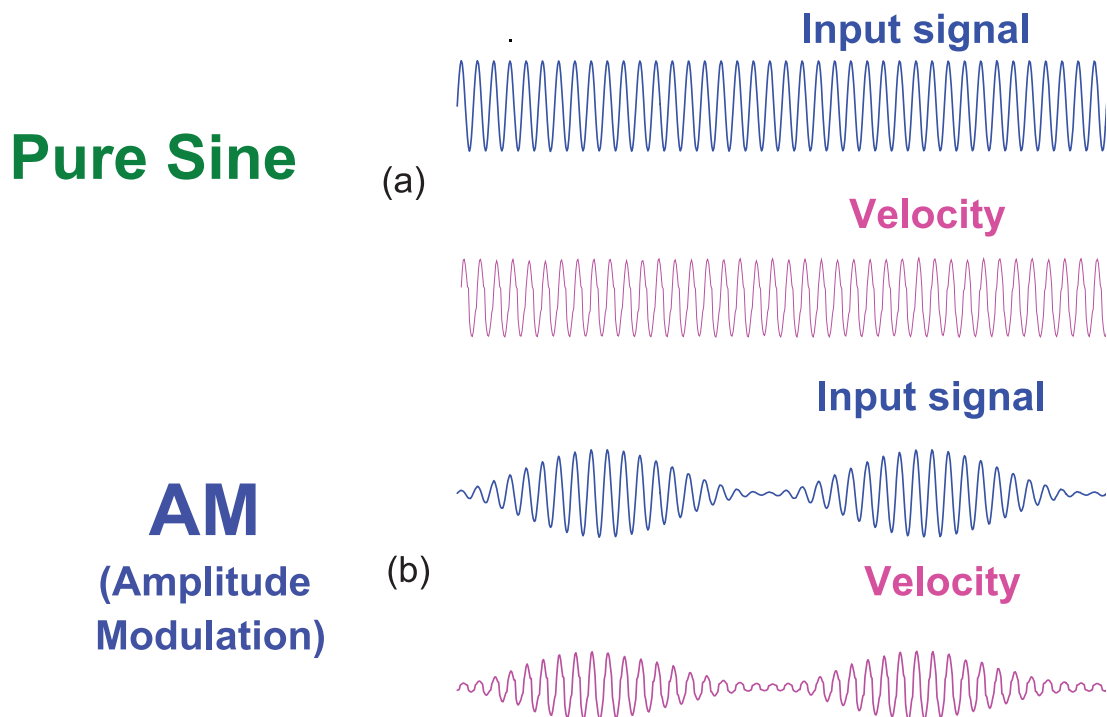


Fig. 6 Actuator calibration response to different excitation signals (from Ref. 11).

through 7e. Figure 7b shows the velocity vectors when the slot exit velocity is zero. The slug of high-velocity fluid (“slug” hereafter, clearly seen in-between the vortices in Figs. 7c-7e and as the red contour in Figs. 8) and the accompanying vortices, associated with the previous cycle, traveled about 3.5 slot widths (h) downstream, while the fluid at the vicinity of the slot is quiescent. At the phase of maximum blowing ($\varphi=90^\circ$, Fig. 7c), a high-velocity fluid slug is ejected from the slot (dominating $y/h < 1$), accompanied by a pair of counter rotating vortices that are just forming and are situated at its sides ($y/h \approx 0.3$ and $x/h \approx \pm 0.8$). In the following phase to be discussed ($\varphi=180^\circ$, Fig. 7d), the slot exit

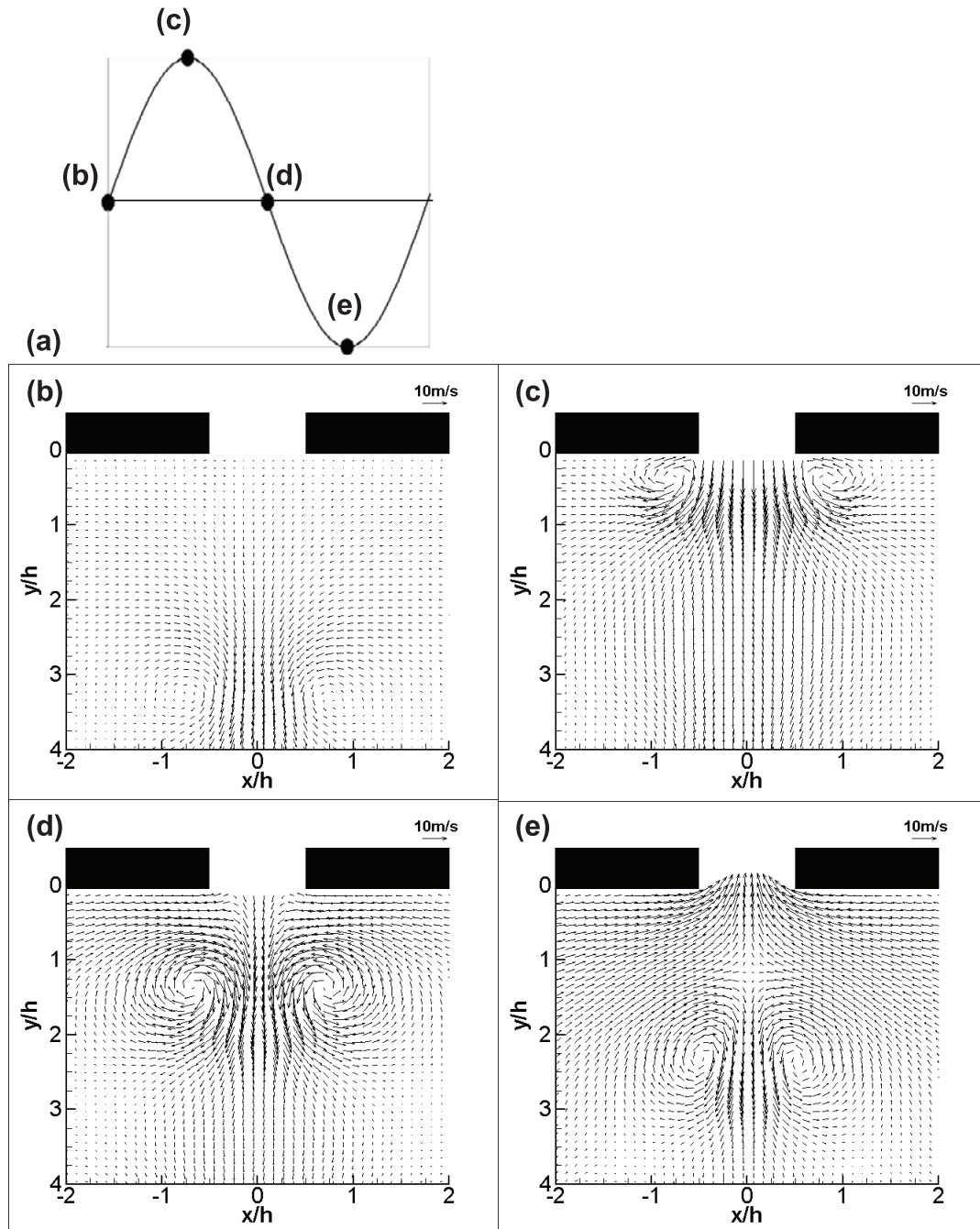


Figure 7. Velocity vectors due to pure sine, wall-normal excitation (90° actuator) ejected into still air. Four phases along the excitation cycle are shown, $f_r=1040\text{Hz}$, $U_p=18\text{m/s}$. $St_{up}=0.06$ and $Re_{up}=1160$.

(a) Schematic velocity signal at slot. The dots indicate phases where data was measured and presented in Figs. 7b-e, (b) $\varphi=0^\circ$, (c) $\varphi=90^\circ$, (d) $\varphi=180^\circ$, (e) $\varphi=270^\circ$.

velocity is still positive at the centerline but negative on the sides and a massive entrainment process takes place between the velocity slug, the vortices (now at $y/h \approx 1.4$) and walls on the sides of the slot. In the last presented phase ($\varphi=270^\circ$, Fig. 7e, peak slot suction), the slug and vortices traveled to $y/h \approx 2.4$, the slug velocity and strength of the vortices have been reduced. A stagnation point flow (as seen in Ref. 4) can be identified in the region bounded by the slot exit and the vortex pair and velocity slug region. The slot region is dominated by the suction induced 2D sink like flow.

Figures 8 and 9 show the corresponding vertical velocity and out-of-plane vorticity contours of the flow fields presented in Figures 7. The first thing to note about the data presented in Figures 8 and 9 is the parallel motion of the ejected slug and the accompanying vortices. The vortices start to form with a small phase lag behind the ejected velocity slug. Figures 9b and 9c clearly demonstrate that the vorticity ejected from the slot (as a result of the in-slot boundary layers) accumulate to form the vortices. While the vortices' peak vorticity and peak velocity in between the vortices lose magnitude as they propagate away from the slot, the vortices get closer due to mutual induction.

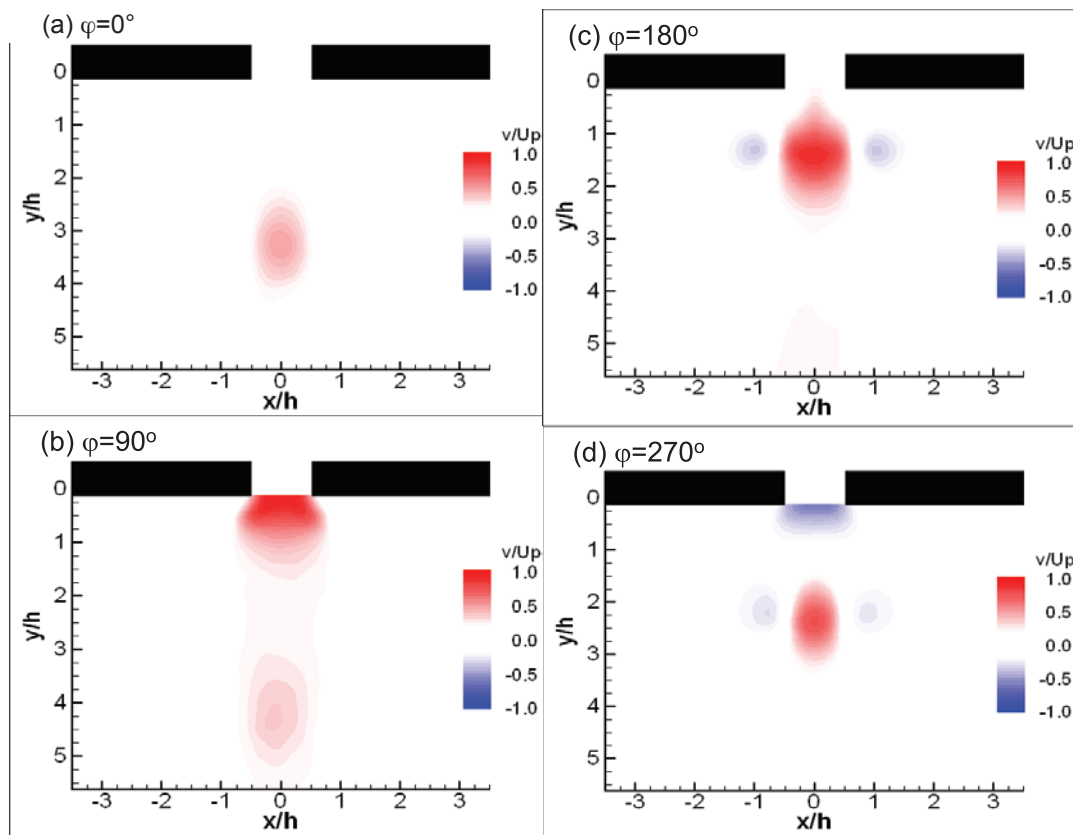


Figure 8. Normalized Vertical Velocity, $U_p=18\text{m/s}$. Conditions as in Fig. 7.

When the peak slot exit velocity is reduced below $U_p=12\text{m/s}$, a different flow field was measured. Figures 10 and 11 show the vertical velocity and vorticity at the phases corresponding to those shown in Figures 8-9, but for $U_p=9\text{m/s}$. As expected, significantly smaller velocities were measured for the ejected slug and suction stages of the cycle ($\varphi=90^\circ$, Figs. 10b and 11b, $\varphi=270^\circ$, Figs. 10d and 11d). The velocity slug did not seem to significantly propagate away from the slot before it disappeared due to the effect of the suction part of the cycle. Two weak vortices were generated at the slot exit (Figs. 10 and 11 b and c), but have *been sucked back into the slot* (Fig. 10d and 11d). Therefore, the still air far field would not sense the effect of the excitation at this sub-critical U_p (i.e., when vortices do not “escape” the vicinity of the slot). The difference between the flow fields presented in Figures 8-9 and those presented in Figures 10-11 could perhaps be appreciated when comparing phases of 90° and 270° for both U_p 's. While in Figure 9b, the vortex-pair started forming and in Figure 9d, it is convected away from the slot, in Figures 11b and 11d we see completely different flow fields in the corresponding

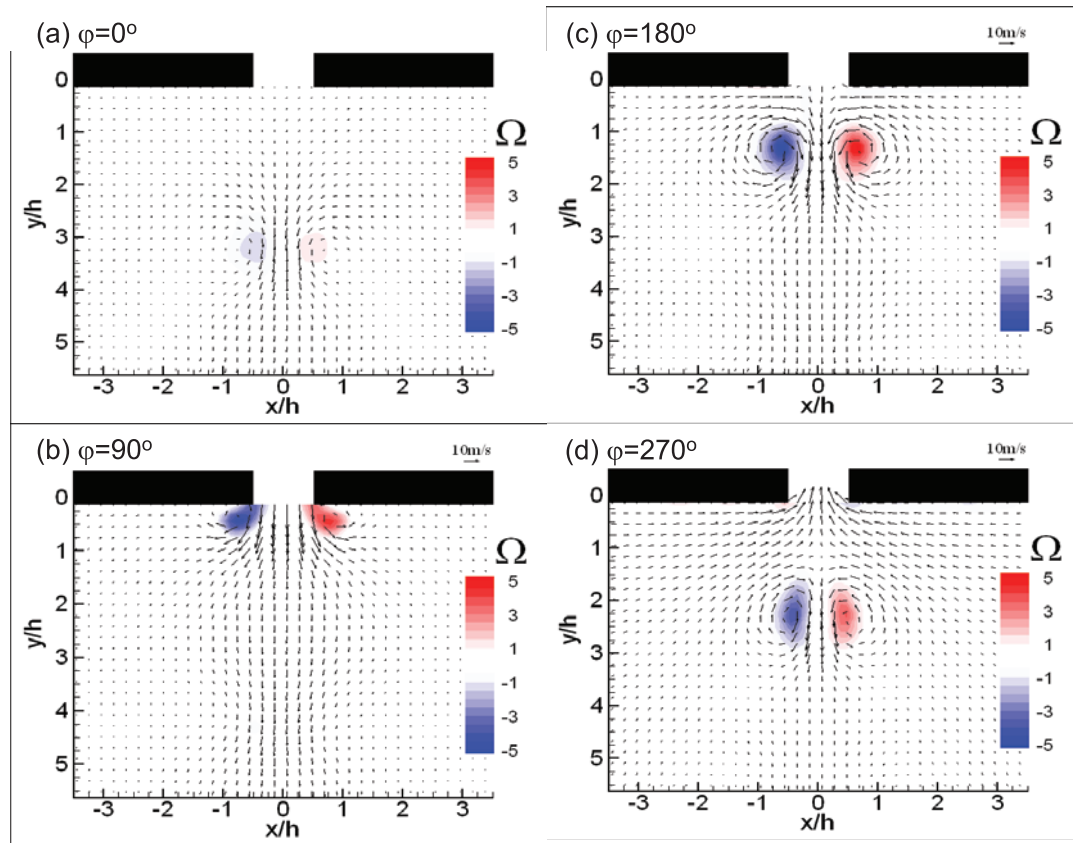


Figure 9. Vorticity Contours (Magnitude truncated), $U_p=18\text{m/s}$. Conditions as in Fig. 7.

phases. Figures 10b and 10d are almost mirror images of one another, i.e. similar magnitudes of the y -velocity component with opposite signs, indicating that this symmetric flow is also linear (since vortices do not “escape”). The resulting *mean* vertical velocity at $y/h=8$ and $x/h=0$ is practically zero for $U_p=9\text{m/s}$ while it is 3.2 m/s for $U_p=18\text{m/s}$. The corresponding mean velocity at the same location was 12m/s for $U_p=43\text{m/s}$ for the compact actuator (Ref. 25).

To better identify the conditions allowing the “escape” of the slug flow and associated vortices from the suction effect, four flow fields measured at times corresponding to the maximum suction velocity at the slot are plotted in Figure 12. This data-set indicates that for the maximum suction phase, the vortices have been sucked back into the slot for $U_p < 11\text{m/s}$. The vortices escape the suction effect and travel an increasingly larger distance away from the slot as the U_p increases (Figures 12d, 12e). This feature is indicative of the highly non-linear and asymmetric nature of the wall-normal excitation resulting flow field, in otherwise still air. It also indicates the dependence of the vortices’ convection speed on U_p . It has been shown [Ref. 32] that the vortices are convected at speeds ranging between 0.21 to 0.29 the peak slot excitation velocity for a huge range of U_p based Reynolds numbers. The conditions under which the vortices escape the slot and their subsequent convection speed, during the time in which the excitation amplitude increases from cycle to cycle (as in AM), are essential to the understanding of the development of amplitude modulated train of vortex pairs ejected into still air. This is because as U_p increases, larger circulation vortices are being generated. The sub-critical vortices do not “escape” the slot and will have no role in the low frequency generation effect on the far field that will be affected only from supercritical vortices. The subsequent vortices are of increasing circulation, therefore of faster convection speed. The faster-stronger vortices can catch-up and interact with weaker-slower vortices to generate fewer vortices for each AM cycle to affect the far-field. During the decreasing part of the AM cycle amplitude, the vortices will be released, as long as they are supercritical and their effect on the far field is weaker. For this reason we should not expect to find a clean harmonic signal at the far-field corresponding to the AM amplitude, but far more complex spectrum that will still be dominated by the AM frequency, as we shall see.

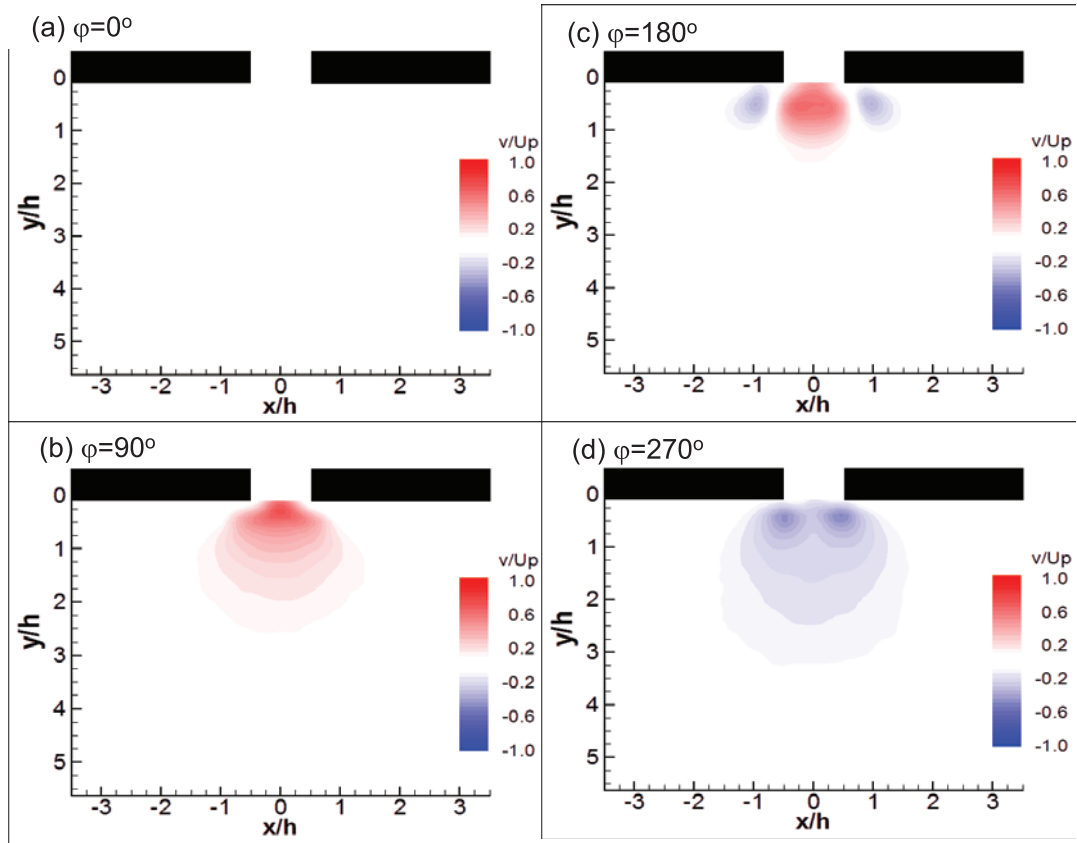


Figure 10. Normalized Vertical Velocity, $U_p=9\text{m/s}$. $St_{up}=0.012$ and $Re_{up}=580$.

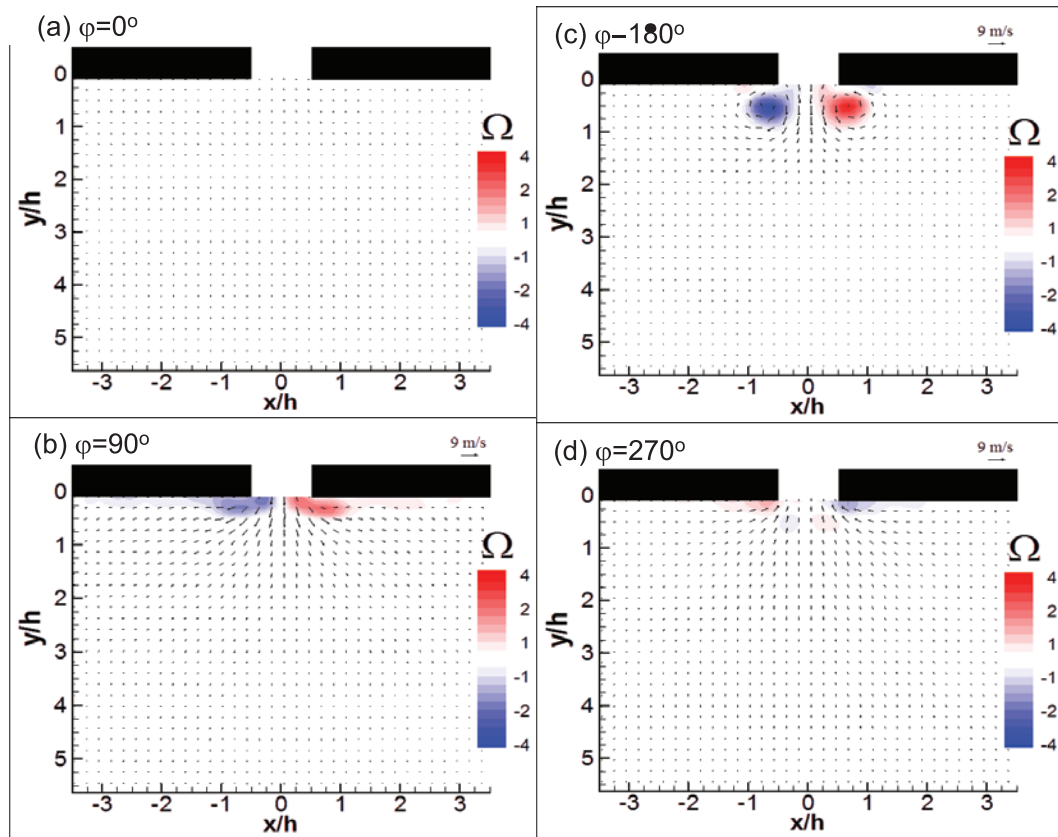
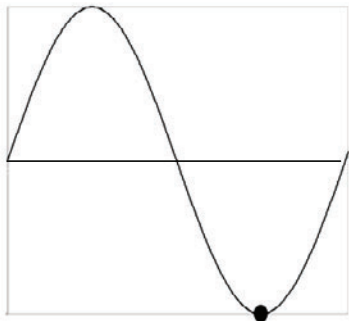
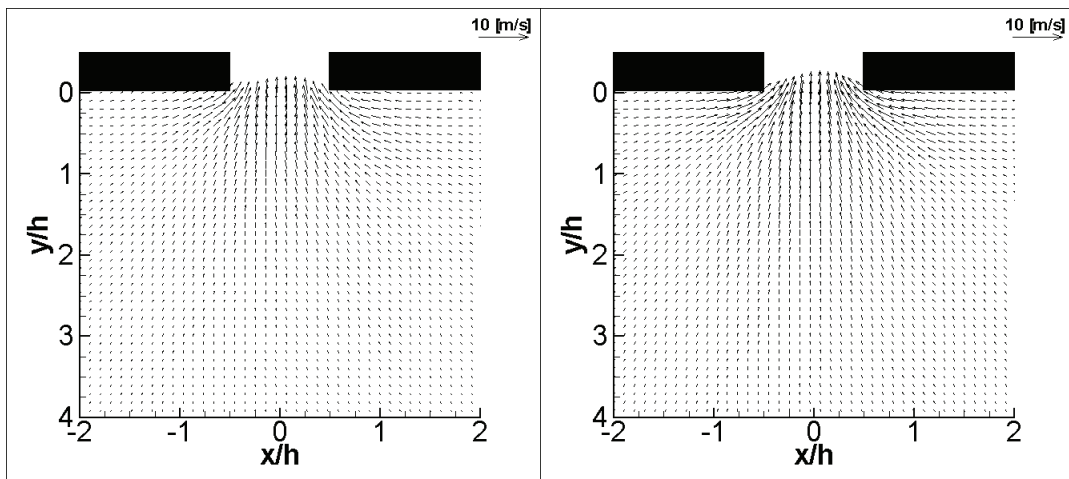


Figure 11. Vorticity Contours (Magnitude truncated), $U_p=9\text{m/s}$. $St_{up}=0.012$ and $Re_{up}=580$.

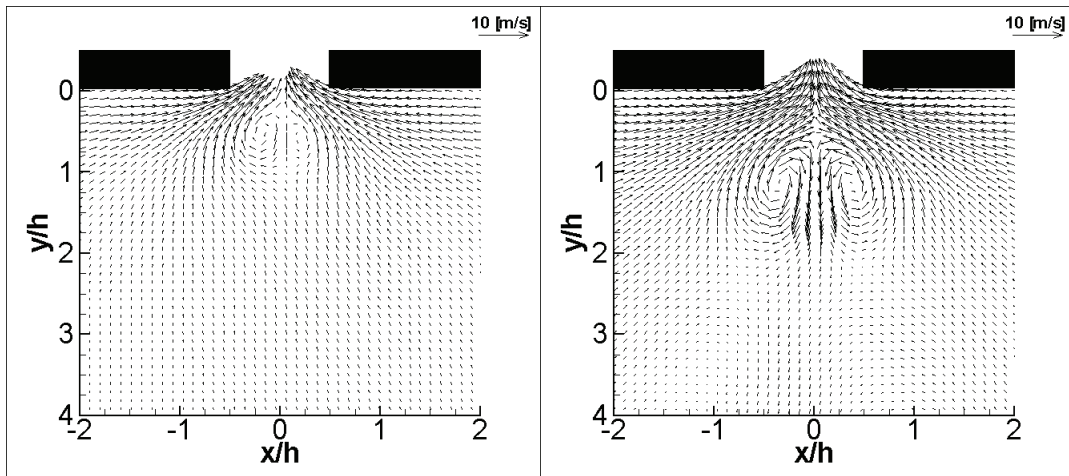


(a) Schematic slot velocity signal showing $\varphi=270^\circ$



(b) $U_p=7.5\text{m/s}$, $St=0.14$, $Re=480$.

(c) $U_p=10.0\text{m/s}$, $St=0.11$, $Re=640$.



(d) $U_p=12\text{m/s}$, $St=0.08$, $Re=800$.

(e) $U_p=15.0\text{m/s}$, $St=0.07$, $Re=970$.

Figure 12. Flow fields measured at phase of maximum slot suction velocity ($\varphi=270^\circ$) for the wall normal excitation in still air. Frequency 1060Hz. U_p , St and Re indicated under each Figure.

Before proceeding with data presentation and discussion, we should introduce the methods used to identify a vortex and calculate its features. Even the definition of a vortex is under some controversy, all the more, its identification method. Historically, vortex identification was performed using dye or smoke flow visualization and the relationship to vorticity dynamics was through hot-wire data and Taylor's hypothesis. Intuitive vortex identification is straightforward when the vortex cross-section is circular and its convection speed has been removed (Ref. 18). In the moving frame of reference, it will be similar to a stationary potential flow point-vortex. Currently, the vortices move in space and significantly change with time, but when coherent, they are easily identifiable either using the peak angular momentum method (AMM, Ref. 19) or by the location of peak vorticity. The angular momentum was calculated for each point in the PIV acquired flow field using four layers that were summed according to the method described in Ref. 25. Unless otherwise noted, the vortices were identified using the AMM (Ref. 19).

The vortex core locations were identified and are plotted in Figure 13a for the three slot exit velocities (i.e., $U_p=9\text{m/s}$, 14m/s and 18m/s , $L_0/h\approx 1.5$, 2.3 and 3.0 , respectively) and for the 90° , plate embedded, wall-normal, actuator operating in still air. The vortex core locations are plotted for all the measured phases (16 per cycle) in which a vortex was identified in the 3mm wide by 4mm long area closest to the slot ($h=1\text{mm}$). The first thing to note about the data shown in Figure 13a is the symmetry of the vortex core locations with respect to the $x=0$ axis. Vortices were first identified for the three slot exit velocities at $y/h\approx 0.25$ and at $x/h\approx \pm 0.75$. Each data point represents a phase increment of 22.5° , while the time base can be inferred from Fig. 13b. The vortices created for $U_p=9\text{m/s}$ do not propagate beyond $y/h\approx 0.5$, rather they are ingested into it. As U_p increases and becomes supercritical, the vortices propagate downstream to increasing distances that are proportional to U_p . The vortices initially (for $t/T < 0.5$) move closer to each other due to at least two possible mechanisms. The first mechanism is related to lower static pressure at the centerline due to acceleration downstream of the stagnation point located between the slot and the velocity slug. The second mechanism is related to induced force acting on a vortex in streaming flow according to potential flow considerations. The vortices are moving away from the $x=0$ axis as they lose coherence and transition to turbulence, towards the end of the first cycle. Exploring the mechanism of the vortices instability and transition mechanism is beyond the scope of the present investigation. Similar results can be found in Visbal et al (Ref. 31) and Smith and Glezer (Ref. 7).

Figure 13b presents the vortices' distance from the slot (y/h locations) vs. time in the excitation cycle. Note that the constant slope of the fitted lines, indicating fixed streamwise convection velocities (U_c), resulting in $U_c=3.0\text{m/s}$ and 4.2m/s for $U_p=14\text{m/s}$ and 18m/s , respectively. When normalizing U_c by U_p , we obtain 0.23 and 0.21 , for $U_p=14\text{m/s}$ and 18m/s , respectively. For the compact actuator (Figure 1), characterized by unrestricted entrainment from essentially the entire plane, with $U_p=43\text{m/s}$, the normalized convection velocity is $U_c/U_p=0.29$, so the convection speed does not simply scale with the slot peak exit velocity. However, the variations are quite small. Since only two U_p levels were measured for the plate normal excitation (90° actuator) using supercritical U_p , it is impossible to determine if there is a trend of U_c/U_p or if the difference is due to experimental uncertainty. Also plotted in Figure 13b are the velocity slug core locations on the $x=0$ axis. It is practically impossible to distinguish these from vortex core streamwise locations. The uncertainty in identifying the locations of the velocity slug and vorticity core are attributed mainly to the size of the interrogation region, which is about $1/50$ the acquisition window size. As could be seen in Fig. 7, this resolution is about 0.1mm .

Next, the circulation of the vortices was calculated, using a surface integral of the vorticity. The integration was performed around the identified vortex cores (using the AMM), down to the lowest closed vorticity contour level that was identified. The circulation is plotted in Figure 13c against the time in the first excitation cycle for the three U_p tested using the 90° , plate embedded, actuator. It can be noted that the vortices are "forming" (gaining circulation) for $t/T < 0.3$. Also, the formation distance is a strong function of U_p , since U_c roughly scales with U_p . For $t/T > 0.4$ the circulation decays, while for $U_p=9\text{m/s}$ the vortex-pair is ingested into the slot with diminished circulation. It seems that the circulation decay rate scales also with U_p , but more data and additional processing is needed to validate this trend. The scaling of the circulation with the slug properties is justified following the accepted norms for vortex rings formation. The slug model (Ref. 21) predicts the vortex circulation as a result of the vorticity flux ejected from the slot neck boundary layers during the ejection period of the cycle. The vorticity flux during the blowing stage of the cycle was calculated and it was found that for the $U_p=18\text{m/s}$ case, the slot exit vorticity flux, calculated from the PIV data at $x/h\approx 0.4$, was $0.046\text{m}^2\text{s}^{-1}$ while from the vorticity surface integral, the maximum calculated circulation was $0.038\text{m}^2\text{s}^{-1}$. This

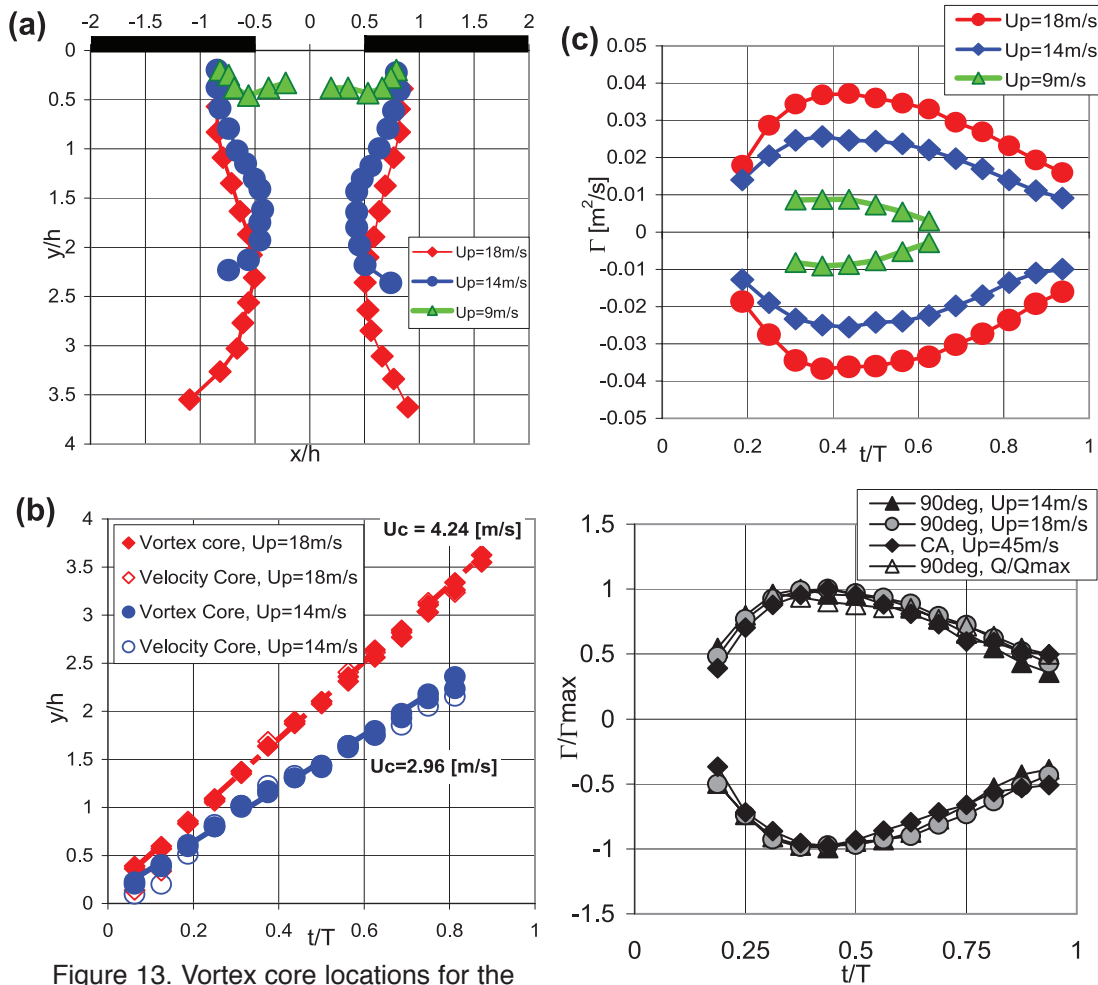


Figure 13. Vortex core locations for the 90° actuator operating in still air and in U_p 's as indicated in legend (a, time can be inferred from 13b), y/h vortex core and velocity slug locations vs. the normalized time (b), and circulation of the vortices vs. the normalized time (c). $Re=580, 800$ and 1160 ; $St=0.12, 0.076$ and 0.059 for $U_p=9, 14$ and 18m/s , respectively.

Figure 13d. Normalized circulation and peak velocities for the compact and 90deg actuators for a range of peak slot exit Reynolds numbers. $Re=900, 1160$ (90deg) and 2900 (CA), $St=0.076, 0.059$ and 0.033 for $U_p=14, 18$ and 45m/s , respectively.

finding indicates that indeed, as also seen in the PIV snapshots (e.g., Figures 9b and 11b), the slot exit boundary layer vorticity rolls up to form the vortices. The fact that the circulation did not saturate (for the compact actuator with $U_p=43\text{m/s}$ the maximum circulation was found to be $0.13\text{m}^2/\text{s}$) as in vortex ring studies (Ref. 23) is encouraging for flow control applications, that will benefit from large vorticity flux and strong vortices ejected from ZMF actuators. This finding also calls for further study to explore the differences between the current findings and the existing vortex ring models that predict saturation of the vortex circulation (e.g., Ref. 23). In Fig. 13d we present the evolution of the normalized vorticity of the two actuator boundary conditions presently used. The almost universal evolution for two different boundary conditions, two frequencies and three slot exit peak velocity Reynolds number justifies the unified discussion to follow.

The effects of Amplitude Modulation

As indicated in the introduction, there is at least an order of magnitude difference between the actuator resonance frequency, where its output is both significant and energy efficient, and the desired significantly lower frequency of actuation. Pulsed modulation (Refs. 29, 6, 11, 22) with extremely low

duty cycles, therefore a proportionally small momentum coefficients, was recently proven very effective flow control approach. However, the evolution of amplitude modulated, burst mode and other complex voltage input signals used to operate ZMF actuators have not been studied in detail previously, to the best knowledge of the authors. Therefore, in order to gain physical insight on the mechanism that creates low-frequency from amplitude modulated high-frequency excitation signal, detailed flow fields were measured, while the actuators operate in still air. Amplitude modulation rather than BM was currently studied since its frequency content is simpler and therefore deemed more suitable for a fundamental study.

We shall start the discussion by considering the operation of the compact actuator (Fig. 1) ejecting the excitation into still air under amplitude modulated excitation. Amplitude modulation is preferred for fundamental studies over other modulated signal waveforms since the slot exit velocity signal is well correlated with the excitation signal.

Figures 14 present vorticity fields corresponding to the peak ejection speed for each high-frequency cycle, in the 5:1 frequency ratio used in this AM case. Figure 14f presents the slot exit peak velocity at every phase of the excitation cycle. It can be seen that four of the five peak slot exit velocities corresponding to four of the five “fast” cycles are supercritical, with $Up,cr \approx 18.8\text{m/s}$ for this case. As seen before for pure sine excitation, as Up increases, stronger and faster vortices are generated. Therefore it is hypothesized that the stronger and faster vortices would accelerate and catch-up with the weaker-slower vortices and either pass through (“leap frog”, Ref. 21) or amalgamate (“pairing”, Ref. 21) with them. In any event, the result would be that the far field would only sense the low frequency content due to the capability of the larger circulation vortices with faster convection speeds to survive for longer distances downstream of the actuator’s slot. The situation is further complicated by the Up threshold, primarily determining the conditions for vortex “escape”, while slower-weaker vortices could be sucked back into the slot. The vorticity data shown in Figures 14a-e corroborate the hypothesis that as the excitation magnitude increases during the AM cycle, the resulting vortices would be stronger (compare Figs. 14a and 14b) and that the y/h distance between two vortex pairs increases as Up increases between Figs. 14b, 14c. The coherence of the vortices is rather poor due to the large slot exit velocity ($Up=35\text{m/s}$ for this case) promoting transition and the additional unsteady effects due to the AM signal.

Figure 15a presents 20 phases along one modulation frequency cycle of an amplitude modulated excitation voltage signal introduced to the compact actuator with $f_r/f_m=5$ (namely, five periods of high frequency cycles – resulting in five vortex pairs with different strength) and $Up=35\text{m/s}$ (with other conditions identical to those of Fig. 14). Figure 15b presents the PIV measured maximum velocity at the actuator’s slot for every phase measured. The critical peak slot exit velocity calculated by the threshold Strouhal number [Ref. 27] is about 18.8m/s. Note that four of the five peak slot exit velocities (corresponding to the possible generation of an “escaped” velocity slug and vortex pair) are higher than $Up=18.8\text{m/s}$. Also the vortex created during the 5th excitation cycle does not seem to convect a significant distance from the slot. Therefore, at least four of the vortices created during every low frequency excitation cycle should be convected downstream and not sucked back into the slot (as shown in Fig. 14). Note also that the 2nd vortex is expected to be the strongest.

Phases $\varphi=0^\circ-72^\circ$ in Fig. 15a correspond to four phases along one high frequency cycle, corresponding to $Up \approx 23.5\text{m/s}$ (each phase of the data in a point in Fig. 15b). One can identify a vortex pair formed and convected downstream. The 1st cycle is followed by a 2nd cycle with larger peak velocity of $Up \approx 35\text{m/s}$, corresponding to phases $\varphi=90^\circ-144^\circ$ in Fig. 15b. As noted before, the larger the peak slot-exit velocity is – the larger the vortex circulation and convection velocity would be. Therefore, the vortex pair formed during $\varphi=90^\circ-144^\circ$ is expected to have larger convection velocity than its predecessor. The second vortex pair indeed moves faster than its predecessor downstream *in a manner that allows the merging of vorticity contours* of the 1st vortex pair formed during $\varphi=0^\circ-72^\circ$ with with the 2nd vortex pair formed at $\varphi=90^\circ-144^\circ$. *This process results in only one vortex pair to be found at $y/h > 4$ after two high frequency excitation cycles. Therefore, it partly explains the low frequency generation mechanism or the demodulation of the AM signal.*

A similar but less pronounced vortex merging takes place with the 3rd vortex pair ($\varphi=162^\circ-216^\circ$), Fig. 15a, even though the peak velocity of this cycle is expected to be lower than the peak velocity of the previous (second) cycle (perhaps indicating that the convection velocities are affected by the interaction and could not assumed to be calculated simply from the pure sine data based and the slot Up). The evolution of the vortex pairs in the following high-frequency cycles (fourth and fifth) is rather

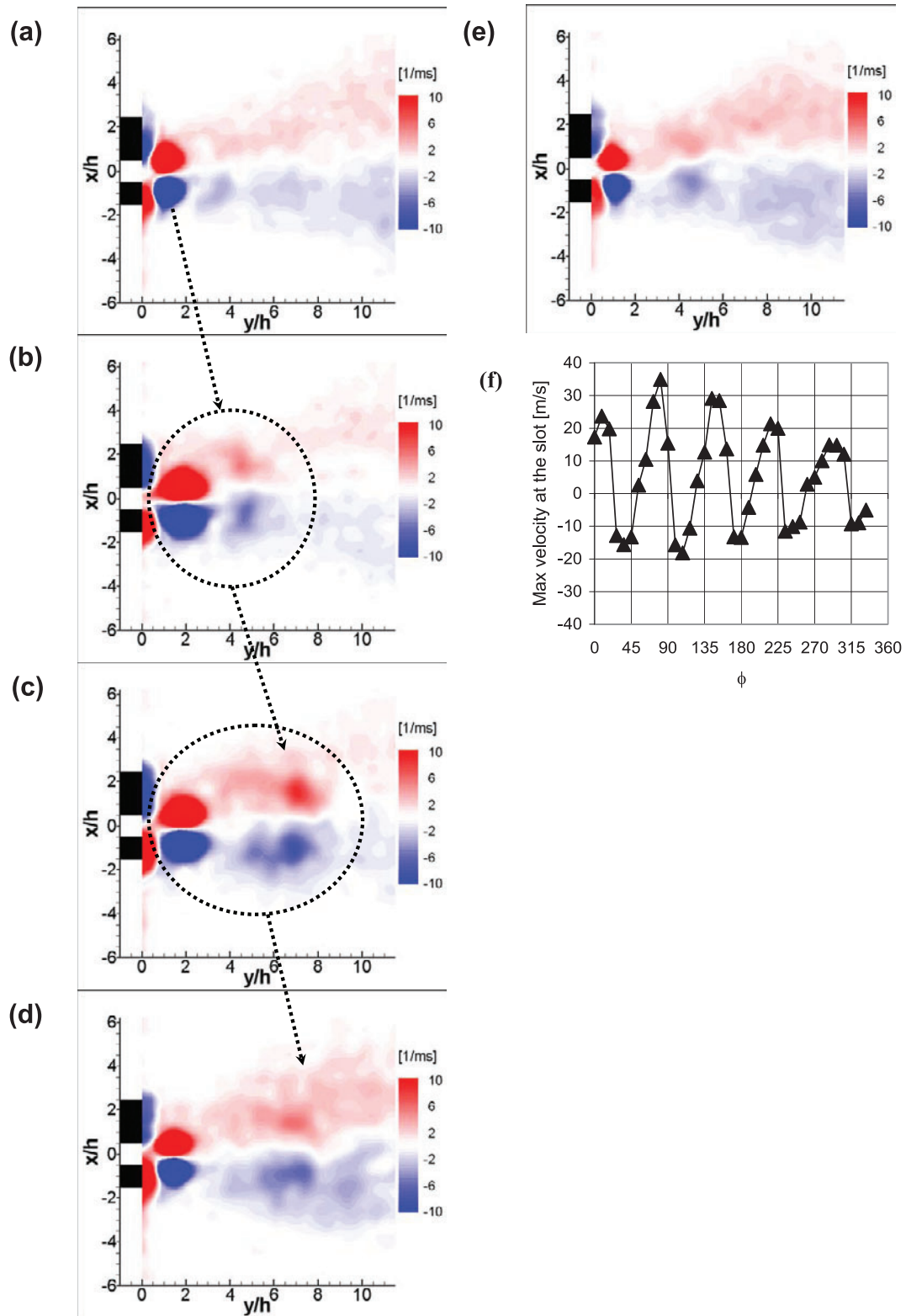


Figure 14. (a-e) Vorticity contours of compact actuator operated by 5:1 frequency ratio AM (1500Hz/300Hz) excitation in still air, $U_p=35m/s$. Phases shown are at 225° of the high frequency signal (carrier). The black regions on the left indicate the compact actuator (CA) slot exit “lips”. (f) Peak velocity measured by PIV near the slot exit. The velocity at the slot is near its minimum for the vortices’ contours shown on the left. $St=0.043$, $Re=2260$.

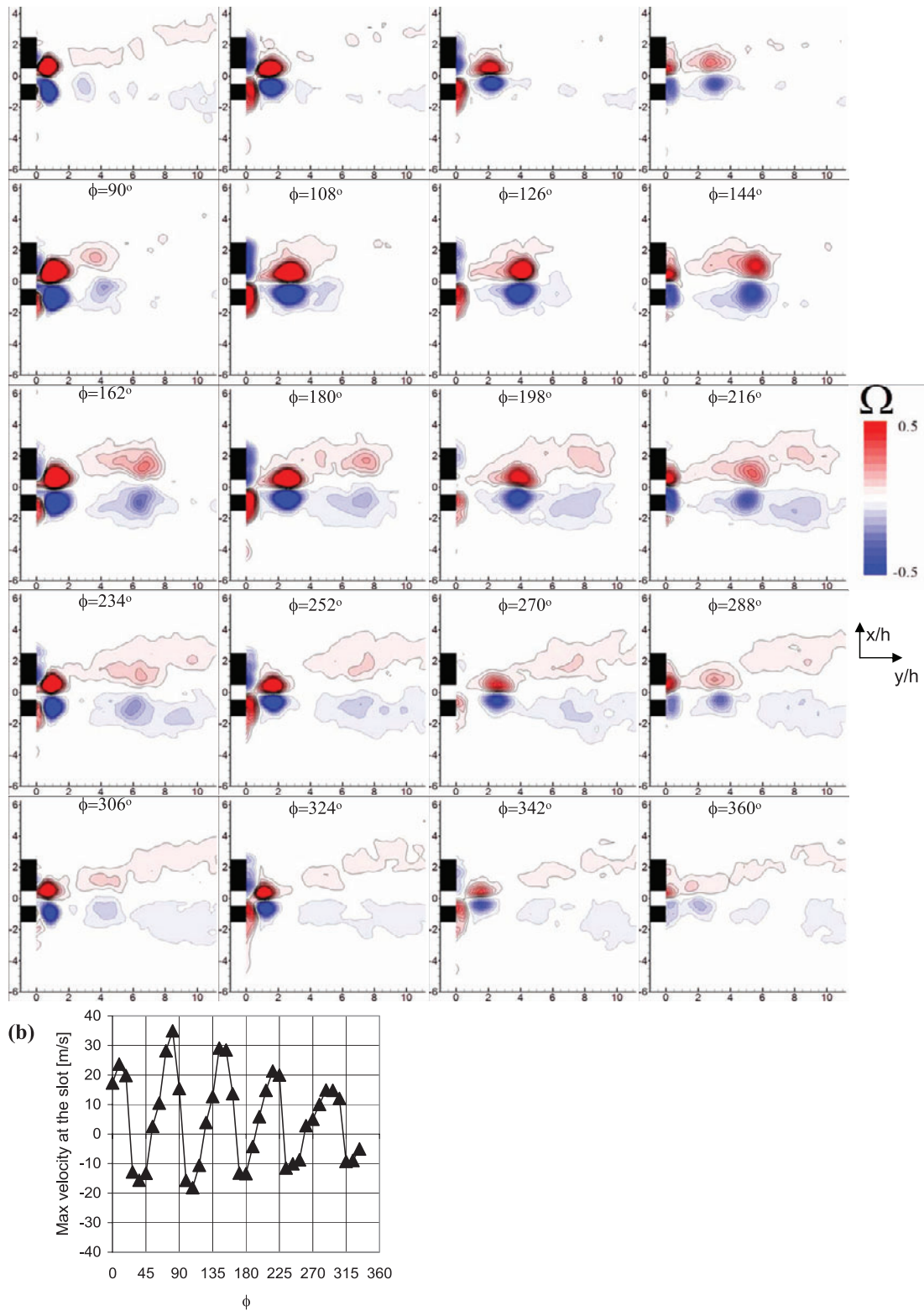


Figure 15. (a) Vorticity field generated by the compact actuator under AM excitation, $f_r/f_m=5$, $U_p=35\text{m/s}$, $f_c=1.5\text{kHz}$. Normalized vorticity contours (truncated to ± 0.5 to magnify effects). $St=0.043$, $Re=2260$. (b) corresponding measured maximum velocity in flow field.

self explanatory and similar to what was seen for pure sine excitation, since no significant (non-linear) interaction takes place there between the subsequent vortex pairs.

Note that the far field senses only one vorticity patch (see phases $\varphi=216^\circ-252^\circ$ at $y/h>4$), where in total five vortex pairs were produced.

The above described process can be summarized as follows: in the rising part of the AM signal (“fast” cycles numbers five, one, and two, Fig. 15a), weaker/slower vortices are followed by stronger/faster vortices that accelerate catch up and “pair” with the previous one. This process results in one big vorticity patch that “survive” rather far from the slot. Whereas for the decreasing part of the AM signal (“fast” cycles three, four, and five), fast/strong vortices are followed by slower/weaker vortices that can not “catch up” and interact with their predecessors, and therefore convect slowly and decay as isolated vortex pairs. Therefore, from the input energy point of view, the decreasing part of the AM input signal is a waste of energy, since in that part of the cycle slower vortices are created that do not contribute to the resulting main far-field vorticity patch. Note that the term vortex is replaced here by vorticity patch, since this vorticity concentration is not as coherent as the vortices that form the vortex pair in the vicinity of the slot.

To further validate the hypothesis regarding pairing, additional data was acquired with the compact actuator operating in still air, at a frequency ratio of 1:10 and $Up\sim 43\text{m/s}$ for the maximum excitation magnitude of the “fast” cycles. The phases to be considered can be depicted by the circle plotted on the excitation signal in Figure 16a. The corresponding vorticity contours are plotted in Figs. 16b-16f. At T1, a vortex pair (marked 1) could be seen to be located at $y/h=3$ (Fig. 16b). By T2 it propagated to $y/h=4$ and a new, stronger and faster, vortex pair (marked 2) can be seen just outside the slot exit, at $y/h=1$ (Fig. 16c). In the following time frame (T3, Fig. 16d), vortex “1” started diffusing and moved to $y/h=5$ while vortex “2” moved to $y/h=1.5$ and gained circulation. Still two closed and separated contours of vorticity could be identified for each vorticity sign vortex in Fig. 16d. At the next time frame (T4, Fig. 16e) the vortices paired to form a single vortex on each side of the x axis, marked by significantly larger circulation, but the core of the new vortex (marked by 2’) did not propagate downstream. At T5, the merged vortex (2’, Fig. 16f) propagated downstream and maintained high circulation. The hot-wire (HW) measured velocity spectra shown in Figure 16g complements the PIV data. Here we present the development of the power spectral density (PSD) vs. y/h on $x=0$. The data presented in Fig. 16f shows how the fluctuation’s energy is transformed from the excitation frequency (f_r) into its side bands and lower harmonics. The spectrum becomes dominated by fm for $y/h>2$.

Next we consider AM (sine envelope) signal emanating from the 90° actuator embedded in a plate and operating in still air. Note that in the previous CA data, all five “fast” cycles generate vortex pairs due to supercritical Up throughout, while in the present case, sub-critical vortices are sucked back into the actuator, adding an additional mechanism for “cleaner” low frequency generation in the far field. This is in addition to the vortex pairing mechanism seen in the case of the compact actuator.

Figures 17a-17e present vorticity contours corresponding to the peak vorticity measured at the proximity of the slot for each high frequency (“fast”) cycle ($\varphi=225^\circ$). The magnitude of the vortices increases from the first through the third (fast) cycles (Figs 17a-17c). For the first, fourth and fifth cycles, the vortices do not escape the suction effect and are ingested back into the slot (this would occur at $\varphi=270^\circ$, see Fig. 12), due to sub-critical Up . Indeed only the vortex pair next to the slot can be seen in Figs. 17a, 17b. In Fig. 17c we can notice the strongest vortex pair just forming and about to amalgamate with the previous vortex (formed in Fig. 17b, second cycle of the high frequency cycle, seen now at $2<y/h<2.5$). The merged vortex moved to $y/h=3$ in the next “fast” cycle (Fig. 17d) and a weaker vortex can be seen next to the slot. The vortices from “fast” cycles 3 and 4 can be seen in the 5th cycle, being convected away from the slot, while a new, weak vortex was formed at the slot but is about to be sucked back into it (Fig. 17e). Figure 17f presents the evolution of the hot-wire spectra for $y/h>1.5$ on $x=0$, where the velocity is always directed away from the slot. The data clearly shows that the AM envelope frequency ($fm=212\text{Hz}$) dominates the far-field spectra together with its harmonics. The excitation frequency ($f_r=1060\text{Hz}$), its side bands ($f_r\pm fm$) and their harmonics (in agreement with the conclusion drawn from Fig. 17e), can be seen as well.

4. CONCLUSIONS

An experimental study, using hot-wires and PIV, was undertaken in order to study the evolution of amplitude modulated excitation of zero-mass-flux actuator in still air. This is a preliminary step in understanding the interaction of such excitation with a cross-flow boundary layer, at least when the

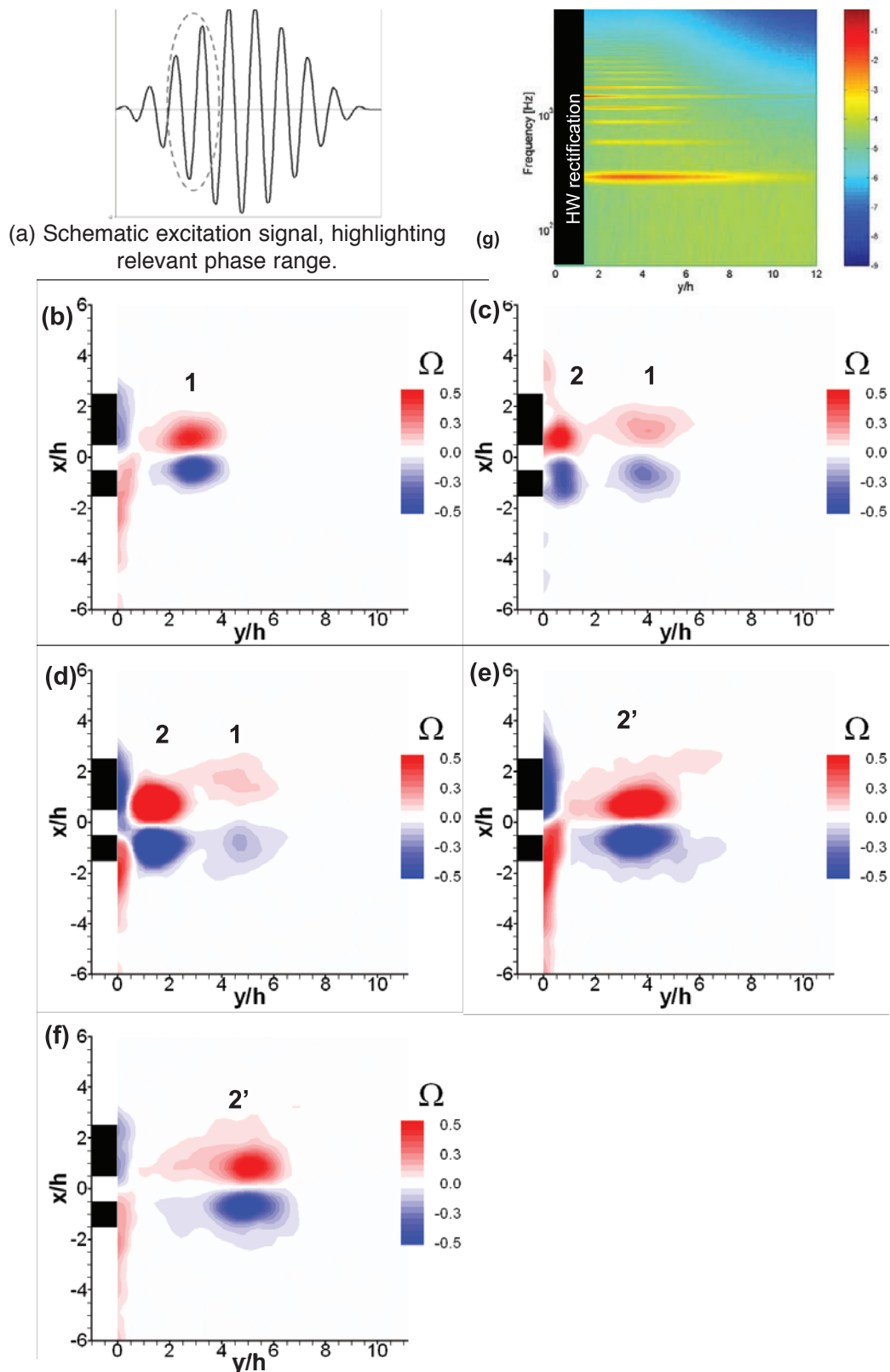


Figure 16. Vorticity of compact actuator operated by 10:1 AM frequency ratio (1500Hz/150Hz) excitation signal in still air. $U_p=43\text{m/s}$. $\Delta\varphi=90^\circ$ (of 1500Hz) between images, showing vortex pairing. The black regions on the left indicate the compact actuator (CA) slot exit "lips". (f) Spectral content of velocity signal measured along the actuator's centerline. $Fr=1500\text{Hz}$, $Fm=150\text{Hz}$. $St=0.035$, $Re=2770$.

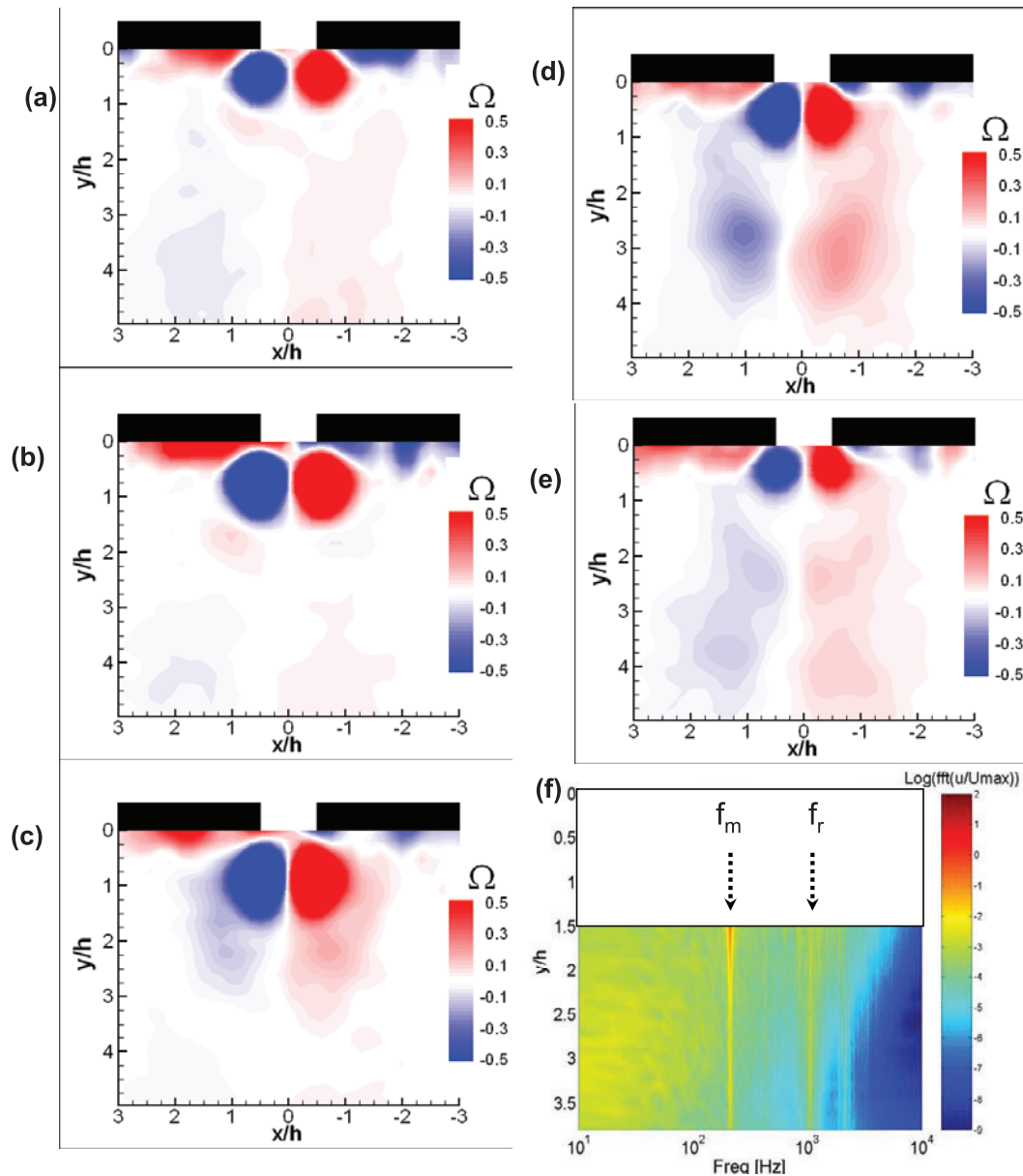


Figure 17. Wall normal (90°) excitation using 5:1 AM input signal (1060Hz/212Hz) Vorticity Contours, $U_p=14\text{m/s}$ operating in *still air*. Phases shown are at 225° of high frequency signal. Where (a) is the “weakest” vortex pair and (c) is the “strongest” vortex pair. The vortices at (a), (d) and (e) are sucked back into the slot. The HW spectra along the y/h axis is shown in (f). Note that for $y/h < 1.5$ the spectra is distorted by HW rectification so it was not presented. $St=0.076$, $Re=900$.

excitation magnitude is of the same order or higher than the free stream velocity. In previous publication it was shown that the vorticity flux from the source (excitation slot) determines the vortex circulation and its subsequent evolution. The peak slot exit velocity determines the (constant) convection speed of the vortices, which is identical to the convection speed of the velocity slug ejected from the slot into quiescent environment. A threshold peak slot velocity exists for vortex “escape” from the suction effect of the slot, in agreement with Holman et al (Ref 27). Sub-critical vortices are sucked back into the actuator and do not effect the far-field.

Low frequency excitation is generated in the near-slot region either through pairing or re-ingestion into the slot of weaker and slower sub-critical vortices. Paring takes place when faster, stronger vortices accelerate towards and amalgamate with preceding slower-weaker vortices. Vortices that are sub-

critical will be sucked back into the actuator and will not affect the far-field. The result of both mechanisms is low frequency excitation, created by one large vortex every low frequency period of the still air at a distance of a few slot widths from the slot.

Acknowledgments

The authors would like to acknowledge the following individuals for the special support to this project: T. Miloh, E. Kronish, M. Vassermann, A. Blas, S. Paster, I. Fono and T. Bachar of the Faculty of Engineering, Tel-Aviv University. Partial support by the Israeli Science Foundation – equipment initiation fund, The Fleischmann, The Meadow, TAU Internal funds and other sources are gratefully acknowledged.

REFERENCES

1. Seifert, A., Darabi, A., Wygnanski, I., "Delay of Airfoil Stall by Periodic Excitation", *Journal of Aircraft*, Vol. 33, No. 4., July-August 1996, pp. 691-698.
2. Gutmark, E.J., Schadow K.C., and Yu, K.H., "Mixing Enhancement in Supersonic Free Shear Flows", *Annu. Rev. Fluid Mech.* 1995, Vol. 27: 375-417.
3. Seifert, A. and Pack, L.G., "Oscillatory Control of Separation at High Reynolds Numbers", *AIAA J.* Vol. 37, No. 9, Sep. 1999, pp. 1062-1071.
4. Smith, B. L., Glezer, A., "The formation and evolution of synthetic jets", *Phys. Fluids*, 31:2281-97, 1998.
5. Pack, L.G. and Seifert, A., "Periodic Excitation for Jet Vectoring and Enhanced Spreading", (AIAA paper 99-0672), *J. Aircraft*, May-June 2001, V38, N3, pp. 486-495.
6. Amitay M., Smith D.R., Kibens, V., Parekh, D.E. and Glezer, A., 2001. "Aerodynamic flow control over an unconventional airfoil using synthetic jet actuators". *AIAA J.* 39, pp. 361-370.
7. Smith, B. L., Glezer, A., "Jet vectoring using synthetic jets", *J. Fluid Mech.*, Vol. 458, 2002, pp. 1-34.
8. Crow, S. C. and Champagne, F. H., "Orderly Structure in jet turbulence", *J. Fluid Mech.* Vol. 48, part 3, 1971, pp. 547-591.
9. Collis, S.S., Joslin, R.D., Seifert, A. and Theofilis, V., "Issues in active flow control: theory, simulation and experiment", *Prog. Aero Sci.*, V40, N4-5, May-July 2004 (previously AIAA paper 2002-3277).
10. Gallas, Q., Mathew, J., Kaysap, A., Holman, R., Nishida T., Carroll B., Sheplak M. and Cattafesta, L., "Lumped Element Modeling of Piezoelectric-Driven Synthetic Jet Actuators", AIAA paper 2002-0125, January 2002.
11. Margalit, S., Greenblatt, D., Seifert, A. and Wygnanski, I., "Active Flow Control of a Delta Wing at High Incidence Using Segmented Piezo-electric Actuators", *AIAA* 2002-3270, June 2002.
12. Ingard, U., Ising, H., "Acoustic nonlinearity of an orifice", *The Journal of Acoustical Society of America*, Vol. 42, No. 1, February 1967, pp. 6-17.
13. Lee, C Y. and Goldstein D B., "Two-Dimensional Synthetic Jet Simulation", *AIAA Journal*, V.40, N.3, March 2002.
14. Mittal, R., Rampunggoon, P., Udaykumar, H. S., "Interaction of a synthetic jet with a flat plate boundary layer", *AIAA* 2001-2773, June 2001.
15. Mittal, R., Rampunggoon, "On the virtual aeroshaping effect of synthetic jets", *Phys. Fluids*, V14, N4, pp.1533-1536 (2002).
16. Park, S-H., Lee, I. and Sung, H. J., "Effect of local forcing on a turbulent boundary layer", *Experiments in Fluids*, V. 31, Issue 4, pp 384-393, 2001.
17. Yehoshua, T. and Seifert, A. "Boundary Condition Effects on Oscillatory Momentum Generator", *AIAA Paper* 2003-3710, June 2003.
18. Adrian R. J., Meinhart, C. D. and Tomkins, C. D., "Vortex organization in the outer region of the turbulent boundary layer", *J. Fluid Mech.* (2000), vol. 422, pp. 1-54.
19. Grosjean, N., Graftieaux, L., Michard, M., Hubner, W., Tropeaz, Volkert, J., Combining LDA and PIV for turbulence measurements in unsteady swirling flows, *Meas. Sci. Technol.* 8 (1997), pp. 1523-1532.

20. Bera, J. C., Michard, M., Grosjean, G., Comte-Bellot, G., "Flow analysis of two-dimensional pulsed jets by particle image velocimetry", *Experiments in Fluids*, Vol. 31, 2001, pp. 519-532.
21. Im, T.T and Nickels, T.B., "Vortex rings", in *Fluid Vortices*, Ed. Green, S.I, Kluwer, 1995, pp. 95-147.
22. Naim, A., Greenblatt, D., Seifert A. and Wygnanski, I., "Active Control of a Circular Cylinder Flow at Transitional Reynolds Numbers" (part of AIAA Paper 2002-3070), special Issue of *Flow, Turbulence and Combustion* on "Air-jet actuators and their use for flow control", (2007), 78: 383-407.
23. M Shusser and M Gharib, "Energy and velocity of a forming vortex ring", *Physics of Fluids*, V 12, N 3 MARCH 2000. pp.618-621.
24. Luton, A, Ragab, S, and Telionis, D, "Interaction of spanwise vortices with a boundary layer", *Physics of Fluids*, V7, N11, 1995, p. 2757.
25. Yehoshua, T., "Boundary Condition Effects on Oscillatory Momentum Generator", MSc thesis, Tel-Aviv University, March 2004).
26. Yehoshua, T. and Seifert, A. "Active boundary layer tripping using oscillatory vorticity generator", in IUTAM Symposium on Laminar-Turbulent Transition : Proceedings of the Sixth IUTAM Symposium on Laminar-Turbulent Transition, Bangalore, India, 2004, Editor: Rama Govindarajan.
27. Holman, R., Cattafesta, L.N., Mittal, R., Smith, B. and Utturkar, Y., "Formation Criterion for Synthetic Jets", *AIAA Journal*, vol. 43, issue 10, pp. 2110-2116 , 2005.
28. Yehoshua, T. and Seifert, A., "Active boundary layer tripping using oscillatory vorticity generator", *Aerospace Science and Technology*, 10 (3): 175-180 APR 2006.
29. Wiltse, J.M. and Glezer, A., "Manipulation of Free Shear Flows using Piezoelectric Actuators," *J. Fluid Mech.*, (1993), 249: 261-285.
30. Cattafesta, L. N. and Sheplak, M., "Actuators for Active Flow Control ", *Ann. Rev. Fluid Mech*, Vol. 43: 247-272, 2011.
31. Rizzetta D. P., Visbal M. R and Morgan, P. E, "A high order compact finite difference scheme for large eddy simulation of active flow control", *Progress in Aerospace Sciences* ISSN: 03760421 Vol: 44 (6) 2008 Page: 397-426.
32. Yehoshua, T. and Seifert, A., "Boundary Condition Effects on the Evolution of a Train of Vortex Pairs in Still Air", *Aeronautical J.*, 110 (1109): 397-417, July 2006.
33. Amitay, M. and Cannelle, F., "Evolution of finite span synthetic jets", *Phys. Fluids* 18, 054101 (2006); doi:10.1063/1.2196093 (16 pages).

